"ViscoRoute": Viscoelastic modeling for asphalt pavements

Denis DUHAMEL
École nationale des Ponts et Chaussées

Armelle CHABOT
Philippe TAMAGNY
Larbi HARFOUCHE
Laboratoire Central des Ponts et Chaussées

INTRODUCTION

The structural role of pavements is to decrease, by means of their material behavior layers, stresses from the supporting soil so as to allow for durable traffic flow and parking. Pavement is composed of a stacking sequence of layers, each performing a distinct function that may be divided into two sub-components: road foundation and surface layers. The road foundation serves to distribute the loads induced by vehicles, bringing them to a level compatible with supporting soil characteristics. This foundation can comprise two sub-layers, called respectively the base course and subbase, which may or may not be distinct in composition depending on both the environment and the traffic intensity applied to the structure. The wearing course, either an overlay or a surface dressing layer, is primarily intended to protect the road foundation against water infiltrations and intense traffic.

The French pavement design method uses Burmister's model [1] for a planar elastic multilayer structure within the half-space composed of the pavement-soil system. This model can be programmed, for example, with LCPC's "ALIZE" software described in Autret *et al.* [2], which yields, in semi-analytical form, the theoretical stress and strain fields taken into account during pavement design. In analyzing certain phenomena not incorporated into conventional tools (e.g. flexible

pavements submitted to either strong temperature gradients or the action of low-speed channeled traffic loads), a real need gets expressed for more highly-specialized numerical tools, for example in coping with slow-moving truck traffic that leads to the appearance at the bottom of the asphalt layer of transverse strains sharply higher than longitudinal strains [3]. This effect, heavily magnified by multiple-load axles (e.g. airport runway loads), is not predicted by conventional computations conducted in elasticity. In the case of laboratory tests on bending cracking, the viscoelasticity of overlays can obviously induce top-down crack propagation, even in the case of a specimen notched over the lower part [4]. Improving model representativeness thus requires, among other things, including the viscoelastic behavior of asphalt overlays.

A semi-infinite multilayer structure model based on Huet and Sayegh's thermoviscoelastic constitutive law [5,6] will be presented herein. The method employed consists, by means of a double Fourier transformation, of setting up the problem within the horizontal wave number space and solving it analytically along the thickness. The solution, identified in the rolling load coordinate system, is obtained by adding a double inverse Fourier transformation outside the coordinate system origin point and applying a special integration technique below this unique point. It then becomes possible to study displacements and stresses at various pavement points vs. loading, temperature or vehicle speed.

COMPUTATION METHOD

The viscoelastic constitutive law

The considered pavement structure is a multilayer half-space composed of layers exhibiting either elastic behavior or thermoviscoelastic behavior characterized by the Huet and Sayegh model, which is particularly well-adapted to asphalt overlays. The rheological behavior model comprises two parallel branches (see Fig. 1): the first represents the viscous part of behavior and contains a spring and two parabolic dampers (with viscosity dependent upon excitation frequency), while the second consists of a spring that corresponds to the static or long-term behavior of the overlay.

E_∞ is the instantaneous elastic modulus, E_0 the static elastic modulus, k and h are the parabolic damper exponents ($1 > h > k > 0$), and δ is a positive adimensional coefficient that accounts for the proportionality between characteristic times of the two dampers. Thermoviscoelastic behavior can thus be characterized, at a given excitation frequency ω (with temporal variation in $e^{-j\omega t}$) and temperature θ, by means of the complex modulus:

$$E^*(\omega,\theta) = E_0 + \frac{E_\infty - E_0}{1+\delta(-j\omega\tau(\theta))^{-k} + (-j\omega\tau(\theta))^{-h}} \qquad (1)$$

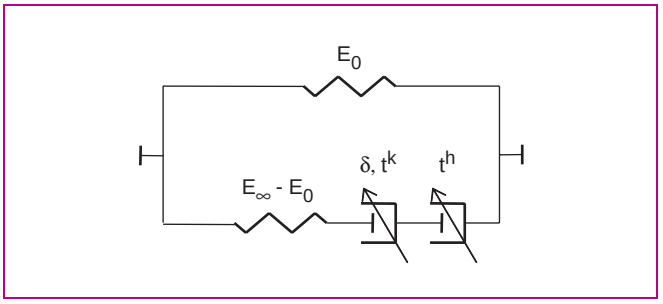

Figure 1
Diagram of Huet and Sayegh's rheological model (1963)

where $\tau(\theta) = \exp(A_0 + A_1\theta + A_2\theta^2)$ is a temperature function that depends upon three scalar parameters A_0, A_1 and A_2, where j is the complex number such that: $j^2 = -1$. In the following discussion, temperature is considered to be uniform and constant by layer, and all indications of the dependence on θ for the various magnitudes can be omitted. Poisson's ratio ν is assumed to be real and independent of the frequency.

Mobile load

The load is assimilated, like in the ALIZE program, with a constant uniform pressure on the rectangle $[-a, a] \times [-b, b]$. It leads to a total loading as $f_0 = 4abp_0$ and moves at a constant speed V (see Fig. 2). In a pavement-related coordinate system, the dynamic equation in each layer *i* is then given by:

$$\mathrm{Div}\left(\sigma(x,y,z,t)\right) = \rho_i \frac{\partial^2 u(x,y,z,t)}{\partial t^2} \qquad (2)$$

where u(x, y, z, t) is the displacement vector, ρi the mass density of the component material of layer *i*, and σ(x, y, z, t) the Cauchy stress tensor. The boundary conditions are expressed as follows:

- on the free surface: $\sigma(z = 0) \cdot n = -p_0 n$ on the rectangle $[-a, a] \times [-b, b]$ and 0 elsewhere, with *n* being the external normal;
- at the interface between layers *i* and *i*+1: $\sigma\left(x,y,z_i^+,t\right)\cdot n = \sigma\left(x,y,z_i^-,t\right)\cdot n$ and $u\left(x,y,z_i^+,t\right) = u\left(x,y,z_i^-,t\right)$ (in the case of perfect bonding, for example);
- at infinity, the fields cancel each other out, i.e. $\sigma(x,y,+\infty,t) = 0$ and $u(x,y,+\infty,t) = 0$.

Inertia forces are generally negligible in pavement applications, yet appear here in order to facilitate the semi-analytical solution to the equations. To make the transition into the mobile coordinate system of the load, the substitution $(x, y, z) \rightarrow (X - \mathbf{V}t, Y, Z)$ is performed, which leads to the following time-independent relation (quasi-stationary mode):

$$\mathrm{Div}\left(\sigma(X,Y,Z)\right) = \rho_i \mathbf{V}^2 \frac{\partial^2 u(X,Y,Z)}{\partial X^2} \qquad (3)$$

The next step consists of taking the Fourier transform of the previous relation in both the X and Y directions. The direct and inverse Fourier transforms of function A are defined by:

$$A^*(k_1,k_2,Z) = \int_{-\infty}^{+\infty}\int_{-\infty}^{+\infty} A(X,Y,Z)e^{-jk_1X}e^{-jk_2Y}dXdY$$
$$A(X,Y,Z) = \frac{1}{4\pi^2}\int_{-\infty}^{+\infty}\int_{-\infty}^{+\infty} A^*(k_1,k_2,Z)e^{jk_1X}e^{jk_2Y}dk_1dk_2 \qquad (4)$$

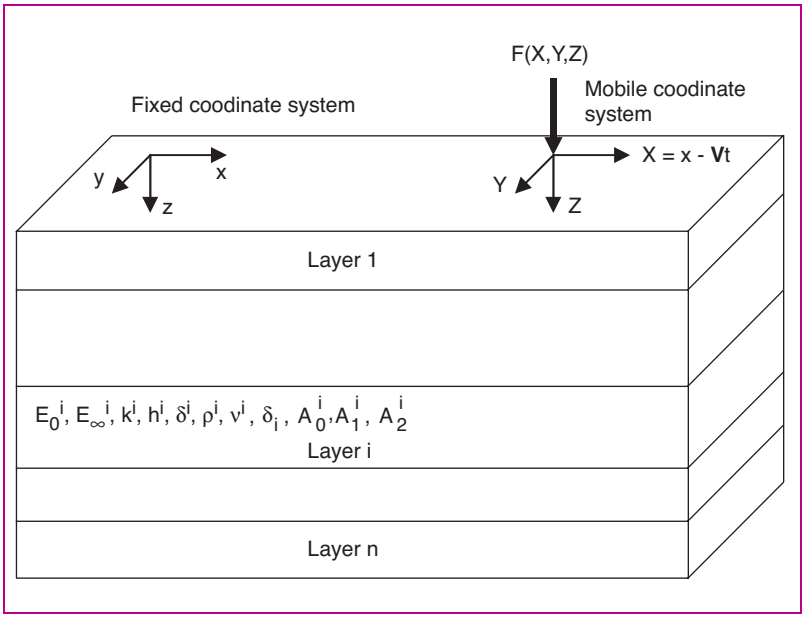

Figure 2
Mobile load on a stratified half-space with the Huet Sayegh model

The constitutive law of each layer *i* can be simply written within the Fourier domain in the multiplicative form:

$$\sigma^*(k_1,k_2,Z) = 2\mu_i^*(k_1V)\varepsilon^*(k_1,k_2,Z) + \lambda_i^*(k_1V)\,\mathrm{tr}\left(\varepsilon^*(k_1,k_2,Z)\right)\mathbf{I} \tag{5}$$

where $\lambda_\iota^*(k_1\mathbf{V})$ and $\mu_\iota^*(k_1\mathbf{V})$ are complex Young's modulus functions $E_\iota^*(k_1\mathbf{V})$ of layer *i* with the same formula as in the elastic case; ε* is the strain tensor. By substituting relation (5) into (3), Nguyen [7] provided, within the wave number domain, the equilibrium relation in each layer *i* in the following form:

$$A_i \frac{\partial^2 \mathbf{U}^*}{\partial Z^2} + jB_i \frac{\partial \mathbf{U}^*}{\partial Z} - C_i U^* = 0 \tag{6}$$

with:

$$A_i = \begin{pmatrix} c_{si}^2 & 0 & 0 \\ 0 & c_{si}^2 & 0 \\ 0 & 0 & c_{pi}^2 \end{pmatrix} \qquad B_i = \begin{pmatrix} 0 & 0 & k_1(c_{pi}^2 - c_{si}^2) \\ 0 & 0 & k_2(c_{pi}^2 - c_{si}^2) \\ k_1(c_{pi}^2 - c_{si}^2) & k_2(c_{pi}^2 - c_{si}^2) & 0 \end{pmatrix}$$

$$C_i = \begin{pmatrix} k_1^2(c_{pi}^2 - \mathbf{V}^2) + k_2^2 c_{si}^2 & k_1 k_2 (c_{pi}^2 - c_{si}^2) & 0 \\ k_1 k_2 (c_{pi}^2 - c_{si}^2) & k_1^2(c_{si}^2 - \mathbf{V}^2) + k_2^2 c_{pi}^2 & 0 \\ 0 & 0 & k_1^2(c_{si}^2 - \mathbf{V}^2) + k_2^2 c_{si}^2 \end{pmatrix} \tag{7}$$

where c_{pi} and c_{si} are the longitudinal and transverse wave speeds respectively in layer *i*. The search for solutions to (6) in the exponential form $\mathbf{U}^*(k_1, k_2, Z) = \mathbf{U}(k_1, k_2)e^{jk3Z}$ leads, in each layer, to the quadratic problem of searching for the following eigenvalues k_3 and eigenvectors **U**:

$$(k_3^2 A + k_3 B + C)\,\mathbf{U}(k_1,k_2) = 0 \tag{8}$$

Ensuring nonzero solutions requires:

$$\det(k_3^2 A + k_3 B + C) = 0 \tag{9}$$

The solutions to this equation are then:

$$\begin{aligned} k_3 &= \pm j\kappa_p \\ k_3 &= \pm j\kappa_s \end{aligned} \tag{10}$$

with the longitudinal and shear wave numbers given by:

$$\kappa_p = \sqrt{(1 - \frac{V^2}{c_p^2})k_1^2 + k_2^2} \text{ et } \kappa_s = \sqrt{(1 - \frac{V^2}{c_s^2})k_1^2 + k_2^2} \tag{11}$$

Six eigenvectors are to be associated with these eigenvalues, which respectively equal:

$$U_{1,2} = \begin{bmatrix} k_1 \\ k_2 \\ \pm j\kappa_p \end{bmatrix} \quad U_{3,4} = \begin{bmatrix} 0 \\ \pm\kappa_s \\ jk_2 \end{bmatrix} \quad U_{5,6} = \begin{bmatrix} \pm\kappa_s \\ 0 \\ jk_1 \end{bmatrix} \tag{12}$$

The first two eigenvectors are associated with κ_p and the remainder with κ_s. The solution to Equation (6) may be written as the sum of these six eigenvectors, which gives rise to an expression of the displacement field in layer *i* that depends on six parameters, denoted $\left(\beta_{1i}^-, \beta_{1i}^+, \beta_{2i}^-, \beta_{2i}^+, \beta_{3i}^-, \beta_{3i}^+\right)$, hence:

$$\begin{aligned}
U_1^* &= k_1\beta_{1i}^- e^{-\kappa_p Z} + \kappa_s\beta_{3i}^- e^{-\kappa_s Z} + k_1\beta_{1i}^+ e^{\kappa_p Z} - \kappa_s\beta_{3i}^+ e^{\kappa_s Z} \\
U_2^* &= k_2\beta_{1i}^- e^{-\kappa_p Z} + \kappa_s\beta_{2i}^- e^{-\kappa_s Z} + k_2\beta_{1i}^+ e^{\kappa_p Z} - \kappa_s\beta_{2i}^+ e^{\kappa_s Z} \\
U_3^* &= j\kappa_p\beta_{1i}^- e^{-\kappa_p Z} + jk_2\beta_{2i}^- e^{-\kappa_s Z} + jk_1\beta_{3i}^- e^{-\kappa_s Z} - j\kappa_p\beta_{1i}^+ e^{\kappa_p Z} \\
&\quad + jk_2\beta_{2i}^+ e^{\kappa_s Z} + jk_1\beta_{3i}^+ e^{\kappa_s Z}
\end{aligned} \tag{13}$$

Displacement is a function of horizontal wave numbers k_1 and k_2 and depth Z. In order to avoid excessive terms in the exponentials, the origin of each layer is chosen at the layer summit. Through use of the relation in (5), the stress tensor can also be written as a function of the six parameters $\left(\beta_{1i}^-, \beta_{1i}^+, \beta_{2i}^-, \beta_{2i}^+, \beta_{3i}^-, \beta_{3i}^+\right)$.

Solution in the multilayer

Displacements and stresses at a given point on the structure may also be expressed in matrix form:

$$\begin{bmatrix} \mathbf{U} \\ \mathbf{t} \end{bmatrix} = \begin{bmatrix} \mathbf{C}_{11} & \mathbf{C}_{12} \\ \mathbf{C}_{21} & \mathbf{C}_{22} \end{bmatrix} \begin{bmatrix} \mathbf{e}^- & 0 \\ 0 & \mathbf{e}^+ \end{bmatrix} \begin{bmatrix} \boldsymbol{\beta}^- \\ \boldsymbol{\beta}^+ \end{bmatrix} \tag{14}$$

where $\mathbf{t} = {}^T[\sigma_{13}\ \sigma_{23}\ \sigma_{33}]$ is the stress vector normal to the horizontal plane. The other vectors and matrices are given by:

$$\boldsymbol{\beta}^- = \begin{bmatrix} \beta_1^- \\ \beta_2^- \\ \beta_3^- \end{bmatrix} \qquad \boldsymbol{\beta}^+ = \begin{bmatrix} \beta_1^+ \\ \beta_2^+ \\ \beta_3^+ \end{bmatrix} \tag{15}$$

$$\mathbf{e}^- = \begin{bmatrix} e^{-\kappa_p Z} & 0 & 0 \\ 0 & e^{-\kappa_s Z} & 0 \\ 0 & 0 & e^{-\kappa_s Z} \end{bmatrix} \qquad \mathbf{e}^+ = \begin{bmatrix} e^{\kappa_p Z} & 0 & 0 \\ 0 & e^{\kappa_s Z} & 0 \\ 0 & 0 & e^{\kappa_s Z} \end{bmatrix} \tag{16}$$

$$\mathbf{C}_{11} = \begin{bmatrix} k_1 & 0 & \kappa_s \\ k_2 & \kappa_s & 0 \\ j\kappa_p & jk_2 & jk_1 \end{bmatrix} \qquad \mathbf{C}_{12} = \begin{bmatrix} k_1 & 0 & -\kappa_s \\ k_2 & -\kappa_s & 0 \\ -j\kappa_p & jk_2 & jk_1 \end{bmatrix} \tag{17}$$

$$\mathbf{C}_{21} = \begin{bmatrix} -2\mu k_1\kappa_p & -\mu k_1 k_2 & -\mu(k_1^2+\kappa_s^2) \\ -2\mu k_2\kappa_p & -\mu(k_2^2+\kappa_s^2) & -\mu k_1 k_2 \\ -j\mu(k_1^2+k_2^2+\kappa_s^2) & -2j\mu k_2\kappa_s & -2j\mu k_1\kappa_s \end{bmatrix} \tag{18}$$

$$\mathbf{C}_{22} = \begin{bmatrix} 2\mu k_1\kappa_p & -\mu k_1 k_2 & -\mu(k_1^2+\kappa_s^2) \\ 2\mu k_2\kappa_p & -\mu(k_2^2+\kappa_s^2) & -\mu k_1 k_2 \\ -j\mu(k_1^2+k_2^2+\kappa_s^2) & 2j\mu k_2\kappa_s & 2j\mu k_1\kappa_s \end{bmatrix} \tag{19}$$

The continuity relations for displacements and stresses are noted at each interface, which yields the following relation between layers *i* and *i*+1:

$$\begin{bmatrix} \mathbf{C}_{11}^i & \mathbf{C}_{12}^i \\ \mathbf{C}_{21}^i & \mathbf{C}_{22}^i \end{bmatrix} \begin{bmatrix} \mathbf{e}_i^- & 0 \\ 0 & \mathbf{e}_i^+ \end{bmatrix} \begin{bmatrix} \boldsymbol{\beta}_i^- \\ \boldsymbol{\beta}_i^+ \end{bmatrix} = \begin{bmatrix} \mathbf{C}_{11}^{i+1} & \mathbf{C}_{12}^{i+1} \\ \mathbf{C}_{21}^{i+1} & \mathbf{C}_{22}^{i+1} \end{bmatrix} \begin{bmatrix} \boldsymbol{\beta}_{i+1}^- \\ \boldsymbol{\beta}_{i+1}^+ \end{bmatrix} \tag{20}$$

where $\bar{\mathbf{e}}_i^{\pm} = \mathbf{e}_i^{\pm}(Z = d_i)$ and d_i is the thickness of layer i. It is preferable to write this relation in the following form:

$$\begin{bmatrix} \boldsymbol{\beta}_i^+ \\ \boldsymbol{\beta}_{i+1}^- \end{bmatrix} = \mathbf{Q}^{i,i+1} \begin{bmatrix} \boldsymbol{\beta}_i^- \\ \boldsymbol{\beta}_{i+1}^+ \end{bmatrix} \tag{21}$$

with the transfer matrix given by:

$$\mathbf{Q}^{i,i+1} = \begin{bmatrix} \bar{\mathbf{e}}_i^- \mathbf{L}_{11}^{i,i+1} \bar{\mathbf{e}}_i^- & \bar{\mathbf{e}}_i^- \mathbf{L}_{12}^{i,i+1} \\ \mathbf{L}_{21}^{i,i+1} \bar{\mathbf{e}}_i^- & \mathbf{L}_{22}^{i,i+1} \end{bmatrix} \tag{22}$$

In this form, transfer matrix **Q** only contains negative exponentials, which serves to avoid possible capacity overages during the computations. Sub-matrices L are expressed as:

$$\begin{aligned}
\mathbf{L}_{11}^{i,i+1} &= -\left[\left(\mathbf{C}_{11}^{i+1}\right)^{-1}\mathbf{C}_{12}^{i} - \left(\mathbf{C}_{21}^{i+1}\right)^{-1}\mathbf{C}_{22}^{i}\right]^{-1}\left[\left(\mathbf{C}_{11}^{i+1}\right)^{-1}\mathbf{C}_{11}^{i} - \left(\mathbf{C}_{21}^{i+1}\right)^{-1}\mathbf{C}_{21}^{i}\right] \\
\mathbf{L}_{12}^{i,i+1} &= \left[\left(\mathbf{C}_{11}^{i+1}\right)^{-1}\mathbf{C}_{12}^{i} - \left(\mathbf{C}_{21}^{i+1}\right)^{-1}\mathbf{C}_{22}^{i}\right]^{-1}\left[\left(\mathbf{C}_{11}^{i+1}\right)^{-1}\mathbf{C}_{12}^{i+1} - \left(\mathbf{C}_{21}^{i+1}\right)^{-1}\mathbf{C}_{22}^{i+1}\right] \\
\mathbf{L}_{21}^{i,i+1} &= \left[\left(\mathbf{C}_{12}^{i}\right)^{-1}\mathbf{C}_{11}^{i+1} - \left(\mathbf{C}_{22}^{i}\right)^{-1}\mathbf{C}_{21}^{i+1}\right]^{-1}\left[\left(\mathbf{C}_{12}^{i}\right)^{-1}\mathbf{C}_{11}^{i} - \left(\mathbf{C}_{22}^{i}\right)^{-1}\mathbf{C}_{21}^{i}\right] \\
\mathbf{L}_{22}^{i,i+1} &= -\left[\left(\mathbf{C}_{12}^{i}\right)^{-1}\mathbf{C}_{11}^{i+1} - \left(\mathbf{C}_{22}^{i}\right)^{-1}\mathbf{C}_{21}^{i+1}\right]^{-1}\left[\left(\mathbf{C}_{12}^{i}\right)^{-1}\mathbf{C}_{12}^{i+1} - \left(\mathbf{C}_{22}^{i}\right)^{-1}\mathbf{C}_{22}^{i+1}\right]
\end{aligned} \tag{23}$$

This process may be pursued until a relation between layers i–1 and i+1 is obtained.

$$\begin{bmatrix} \boldsymbol{\beta}_{i-1}^+ \\ \boldsymbol{\beta}_{i+1}^- \end{bmatrix} = \mathbf{Q}^{i-1,i+1} \begin{bmatrix} \boldsymbol{\beta}_{i-1}^- \\ \boldsymbol{\beta}_{i+1}^+ \end{bmatrix} \tag{24}$$

with the new transfer matrix written as:

$$\begin{aligned}
\mathbf{Q}_{11}^{i-1,i+1} &= \mathbf{Q}_{11}^{i-1,i} + \mathbf{Q}_{12}^{i-1,i}\mathbf{R}_a^i\mathbf{Q}_{11}^{i,i+1}\mathbf{Q}_{21}^{i-1,i} \\
\mathbf{Q}_{12}^{i-1,i+1} &= \mathbf{Q}_{12}^{i-1,i}\mathbf{R}_a^i\mathbf{Q}_{12}^{i,i+1} \\
\mathbf{Q}_{21}^{i-1,i+1} &= \mathbf{Q}_{21}^{i,i+1}\mathbf{R}_b^i\mathbf{Q}_{21}^{i-1,i} \\
\mathbf{Q}_{22}^{i-1,i+1} &= \mathbf{Q}_{21}^{i,i+1}\mathrm{R}_b^i\mathbf{Q}_{22}^{i-1,i}\mathbf{Q}_{12}^{i,i+1} + \mathbf{Q}_{22}^{i,i+1}
\end{aligned} \tag{25}$$

with $\mathbf{R}_a^i = \left(1 - \mathbf{Q}_{11}^{i,i+1}\mathbf{Q}_{22}^{i-1,i}\right)^{-1}$ and $\mathbf{R}_b^i = \left(\mathbf{1} - \mathbf{Q}_{22}^{i-1,i}\mathbf{Q}_{11}^{i,i+1}\right)^{-1}$. This step is concluded by deriving a relation between parameters of the first and last layers:

$$\begin{bmatrix} \boldsymbol{\beta}_1^+ \\ \boldsymbol{\beta}_n^- \end{bmatrix} = \mathbf{Q}^{1,n} \begin{bmatrix} \boldsymbol{\beta}_1^- \\ \boldsymbol{\beta}_n^+ \end{bmatrix} \tag{26}$$

The condition at infinity is:

$$\boldsymbol{\beta}_n^+ = 0 \tag{27}$$

Relation (26) can actually be represented as:

$$\boldsymbol{\beta}_1^+ = \mathbf{Q}_{11}^{1,n}\ \boldsymbol{\beta}_1^- \tag{28}$$

The boundary condition on the upper surface yields:

$$\begin{bmatrix} \mathbf{C}_{21}^1 & \mathbf{C}_{22}^1 \end{bmatrix} \begin{bmatrix} \boldsymbol{\beta}_1^- \\ \boldsymbol{\beta}_1^+ \end{bmatrix} = \mathbf{f} \tag{29}$$

with the loading vector given by:

$$\mathbf{f}(k_1,k_2)=\frac{4\sin(k_1a)\sin(k_2b)}{k_1k_2}\mathbf{f}_0 \tag{30}$$

where $\mathbf{f}_0$ is a constant vector indicating the load application direction, often along the normal, yet tangential loadings are also possible, e.g. braking forces or centrifugal forces. Relations (28) and (29) enable computing the amplitudes β within the initial layer. These are given by:

$$\begin{aligned}\boldsymbol{\beta}_1^- &= \left[\mathbf{C}_{21}^1+\mathbf{C}_{22}^1\mathbf{Q}_{11}^{1,n}\right]^{-1}\mathbf{f}\\ \boldsymbol{\beta}_1^+ &= \mathbf{Q}_{11}^{1,n}\left[\mathbf{C}_{22}^1\mathbf{Q}_{11}^{1,n}+\mathbf{C}_{21}^1\right]^{-1}\mathbf{f}\end{aligned} \tag{31}$$

The amplitudes in the other layers can next be obtained from (21):

$$\begin{aligned}\boldsymbol{\beta}_{i+1}^- &= \left[\mathbf{1}-\mathbf{Q}_{22}^{i,i+1}\mathbf{Q}_{11}^{i+1,n}\right]^{-1}\mathbf{Q}_{21}^{i,i+1}\boldsymbol{\beta}_i^-\\ \boldsymbol{\beta}_{i+1}^+ &= \mathbf{Q}_{11}^{i+1,n}\left[1-\mathbf{Q}_{22}^{i,i+1}\mathbf{Q}_{11}^{i+1,n}\right]^{-1}\mathbf{Q}_{21}^{i,i+1}\boldsymbol{\beta}_i^-\end{aligned} \tag{32}$$

The displacement and stress fields within the wave number domain have, at this point, been determined. It should be noted that the matrix operations displayed in the previous equations pertain solely to matrices relatively small in size; these operations can thus be conducted as is, without relying upon any dedicated numerical algorithms. A return to the domain of space variables (X, Y, Z) entails use of the inverse Fourier transform.

THE "VISCOROUTE" SOFTWARE APPLICATION

Numerical computation

Computation is based on executing numerical FFT (fast Fourier transform) operations. The computed magnitude depends on longitudinal wave numbers k_1 and k_2, which may be written in the form $f(k_1,k_2)$. An inverse Fourier transformation using FFT yields the same magnitudes in the real domain, a step that requires discretizing function f by taking discrete values in the following form:

$$f(i_1\delta k_1, i_2\delta k_2) \text{ avec } -\frac{N_1}{2}<i_1\le\frac{N_1}{2} \text{ et } -\frac{N_2}{2}<i_2\le\frac{N_2}{2} \tag{33}$$

N_1 is selected such that:

$$\left(\sum_{i_1=1}^{i_1=5}\left|f(-\frac{N_1}{2}\delta k_1+i_1\delta k_1,0)\right|\right)<\varepsilon\left(\sum_{i_1=1}^{i_1=5}\left|f(i_1\delta k_1,0)\right|\right) \tag{34}$$

This expression signifies that function values are small at the left-hand extremity over the discretized domain. The same procedure is also applied to choose N_2. The value of ε is set equal to 10^{-3}. A discrete Fourier transformation is then carried out to obtain:

$$f(i_1\delta x_1, i_2\delta x_2) \text{ avec } -\frac{N_1}{2}<i_1\le\frac{N_1}{2} \text{ et } -\frac{N_2}{2}<i_2\le\frac{N_2}{2} \tag{35}$$

which is the computed value in the real domain at the desired depth, with the result: $\delta x_1 = 2\pi/(\delta k_1 N_1)$. To ensure validity of the solution derived, the following is to be verified:

$$\left(\sum_{i_1=1}^{i_1=5}\left|f(-\frac{N_1}{2}\delta x_1+i_1\delta x_1,0)\right|\right)<\tilde{\varepsilon}\left(\sum_{i_1=1}^{i_1=5}\left|f(i_1\delta x_1,0)\right|\right) \tag{36}$$

where $\tilde{\varepsilon}$ is a small-valued parameter. Otherwise, δk_1 is replaced by $\delta k_1/2$ and the computation is reinitiated. The same steps apply to verify that δk_2 has been selected at a low enough value.

The computation of $f(i_1\,\delta k_1, i_2\delta k_2)$ is performed rather smoothly except for $i_1 = 0$, since function f is unique for $k_1 = 0$. In order to overcome this difficulty, $f(0,i_2\delta k_2) = 0$ is imposed prior to conducting the FFT on this modified function. Corrections are then introduced in the real domain by adding the missing part around $k_1 = 0$ to the resultant function, hence:

$$f(i_1\delta x_1, i_2\delta x_2) = f_{FFT}(i_1\delta x_1, i_2\delta x_2) + FFT_{k_2}\left[\int_{-\frac{\delta k_1}{2}}^{\frac{\delta k_1}{2}} f(k_1,k_2)dk_1\right] \qquad (37)$$

For the sake of simplification, the corrective term is set constant along direction 1 and its corresponding FFT is set on variable 2 alone. This procedure makes it possible to improve the solution and thereby avoid having to assign very high values for N_1 and N_2.

Graphics interface

The above computations were programmed with a software package called "ViscoRoute", which is composed of a computation module written in C++ and an input-output interface written in Visual Basic®. A sample input configuration has been shown in Figure 3. The upper part of the window focuses on defining the properties of the various material layers (both behavior and geometry), while the lower part serves to define the loading and potential output type. The parameters to be introduced have been listed in Table I. Figure 4 provides an example of results visualization; it is possible to plot the output magnitude along an axis parallel to the *x* or *y* axis. Visualization in the form of a surface as a function of *x* and *y* is also permitted. Output parameters could consist of the three-directional displacements, the six strain tensor components, the six stress tensor components, the three displacement vector components, or the three acceleration vector components.

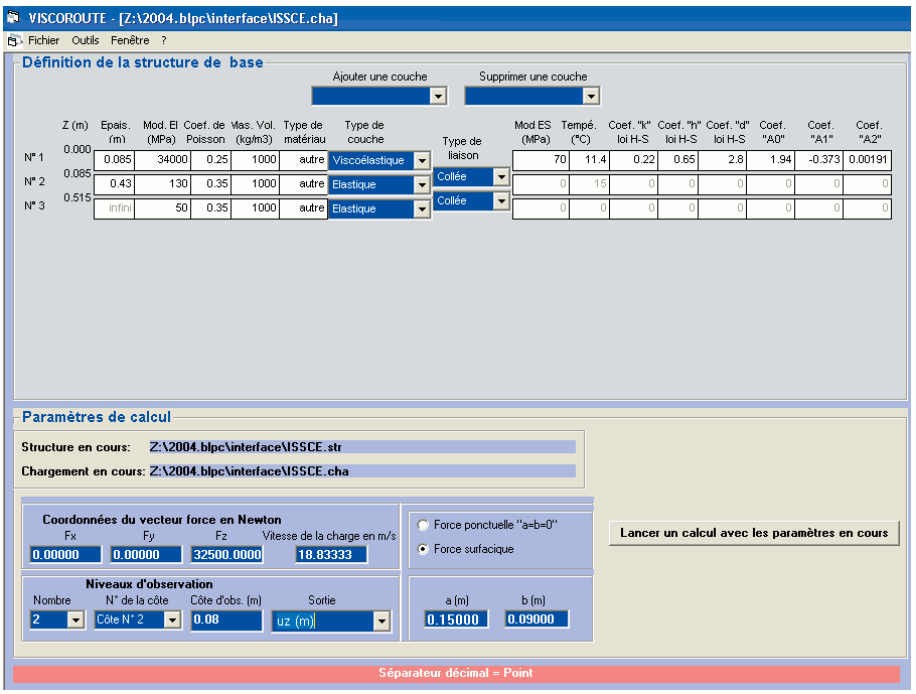

Figure 3
Input of structure and loading parameters

TABLE I
ViscoRoute input parameters

Parameters	Summary comments on the data
F_X, F_Y, F_Z, V	Total force vector coordinates, in newtons, and load speed, in m/sec
Force option a, b	*Force option*: two Boolean values are possible: 1: either the case of a point force (a = b = 0) 2: or the case of a surface force, with values *a* and *b* being those of the target surface (2a × 2b)
N	Number of layers (≥ 1)
For all $1 \le i \le N$ $\begin{cases} \rho_i & E_i^\infty & \nu_i & d_i & c_i \\ opt & E_0^i & k_i & h_i & \delta_i \\ \theta_i & A_0^i & A_1^i & A_2^i & \end{cases}$	ρ_i: mass density E_i^∞ : instantaneous elastic modulus ν_i: Poisson's ratio d_i: layer thickness c_i: type of bonding with the lower layer (0-bonded, 1-sliding layer) opt: type of layer (0-elastic, 1-thermoviscoelastic) E_0^i : static elastic modulus k_i: coefficient used in the Huet and Sayegh Law h_i: coefficient used in the Huet and Sayegh Law δ_i: coefficient used in the Huet and Sayegh Law θ_i: temperature A_0^i , A_1^i , A_2^i : evolution law coefficients with resepct to temperature
m	Number of points at which the result is computed
Depth (i) $1 \le i \le m$	*Depth* (i): positive real number representing the depth at which output is to be studied
Output (i) $1 \le i \le m$	*Type of desired output*: displacement: u_x, u_y, u_z strain: ε_{xx}, ε_{yy}, ε_{zz}, ε_{yz}, ε_{xz}, ε_{xy} stress: σ_{xx}, σ_{yy}, σ_{zz}, σ_{yz}, σ_{xz}, σ_{xy} speed: v_x, v_y, v_z acceleration: a_x, a_y, a_z

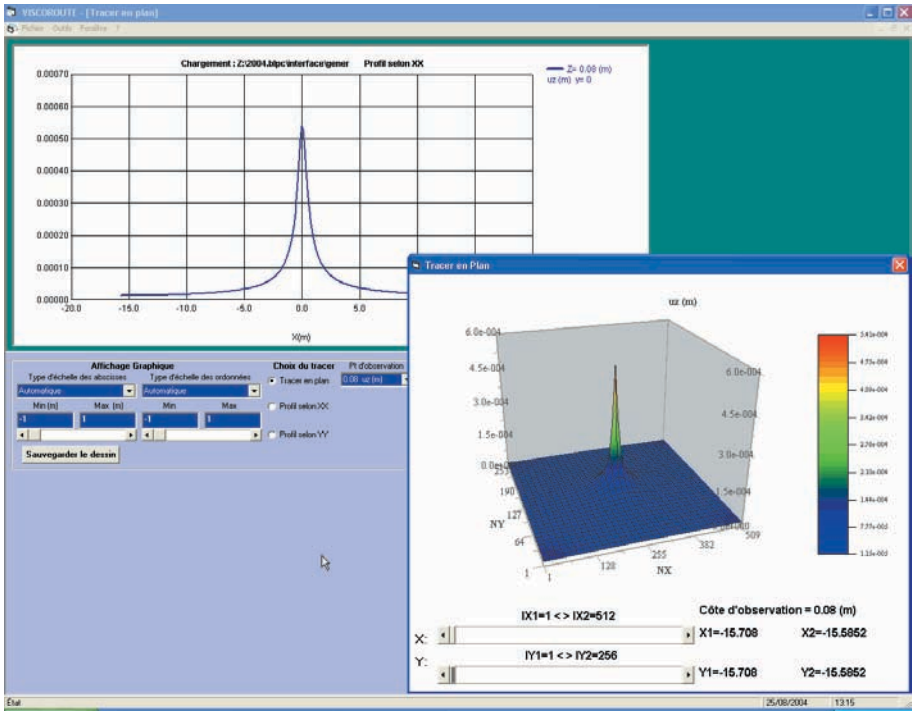

Figure 4
Example of displacement in the z-direction

EXAMPLES

In what follows, we will present a few examples of results and comparisons with other methods, either analytical or numerical (see also [8,9]). The loading is a 65-kN mobile force distributed over a square surface with side lengths 2a = 2b = 0.22158 m (1/2 the standard axle in road design). Except for specifications stating otherwise, load speed equals 5 m/sec. The parameters inherent in the complex modulus of viscoelastic materials are obtained from standardized bending test results on a trapezoidal bracket specimen (NF P 98-261-1). The Huet and Sayegh model parameters based on complex modulus test results can be determined using the "ViscoAnalyse" software developed in a Matlab® environment [10].

Parameters of the temperature function $\tau(\theta)$ for the bitumen-bound granular material subsequently chosen are: $A_0 = -0.342$, $A_1 = -0.401$, $A_2 = 0.002954$, and the temperature θ is 15°C.

Homogeneous half-space

The first example entails studying the mechanical fields in a half-space with assumed linear elastic behavior. The elasticity constants are obtained from a viscoelastic material featuring a Poisson's ratio of 0.35, an instantaneous modulus $E_\infty = 29{,}914$ MPa and a deferred modulus $E_0 = 70$ MPa. Damper parameters are assumed such that $\delta = 0$ and $h = 0$. The target material is thus equivalent to an elastic material with a Young's modulus of 14,992 MPa. The second case is a material displaying the same parameters, except that coefficient h now equals 0.3 in order to ascribe the material a viscoelastic behavior. Curves in Figures 5 and 6 show the vertical displacement for depths z1 = –0.0165 m and z2 = –0.2444 m. The comparisons with Boussinesq's analytical solution given in [11] and the semi-analytical solution obtained in [12] for the viscoelastic case are both excellent (i.e. differences of less than 1%).

Multilayer

The second comparison has been shown in Figure 7. The structure contains a viscoelastic layer of a virtual material 8 cm thick with the following mechanical characteristics ($\nu = 0.35$, $E_0 = 0$, $E_\infty = 29{,}914$ MPa, $h = 0.5$, $\delta = 0$). This layer lies on both an elastic layer 24 cm thick ($\nu = 0.35$, $E = 10{,}000$ MPa) and an elastic solid ($\nu = 0.35$, $E = 50$ MPa). The comparison is drawn by finite element computation via the CVCR modulus contained in the CESAR-LCPC code [13]. In this finite

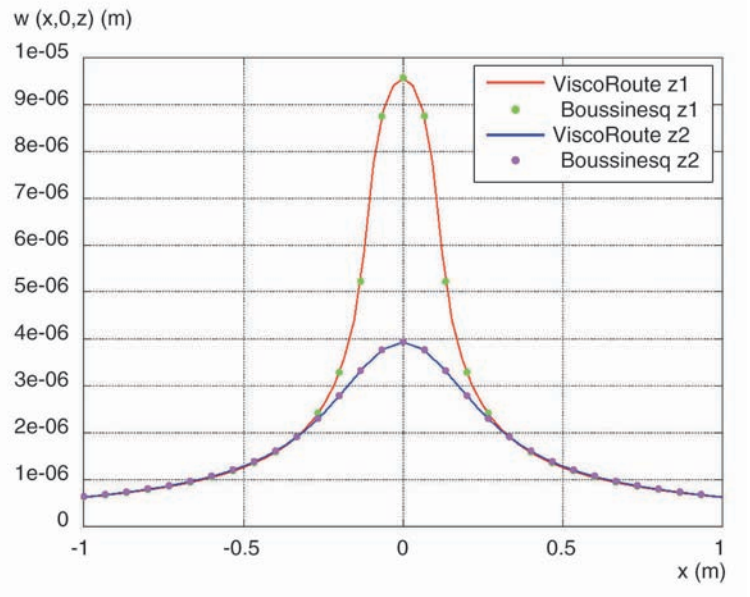

Figure 5
Displacements for an elastic half-space with δ = 0, h = 0 and for depths z1 = – 0.0165 m and z2 = – 0.2444 m

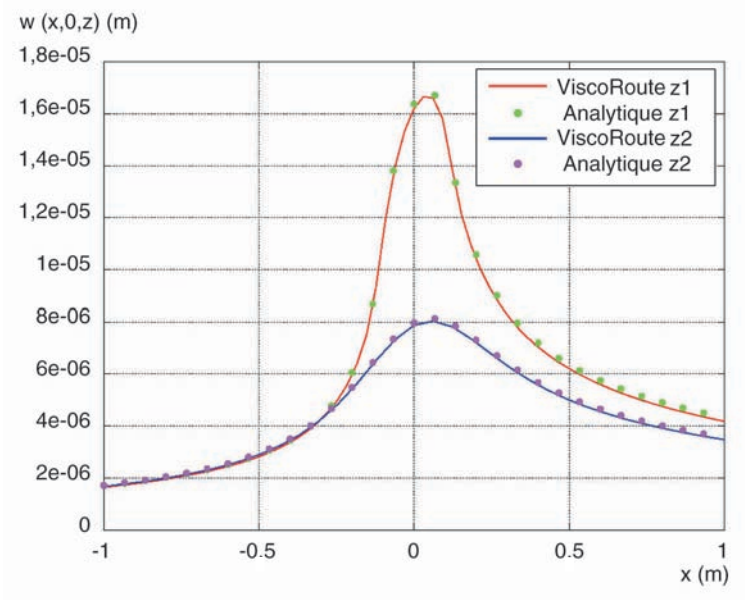

Figure 6

Displacements for a viscoelastic half-space with δ = 0, h = 0.3 and for depths z1 = – 0.0165 m and z2 = – 0.2444 m

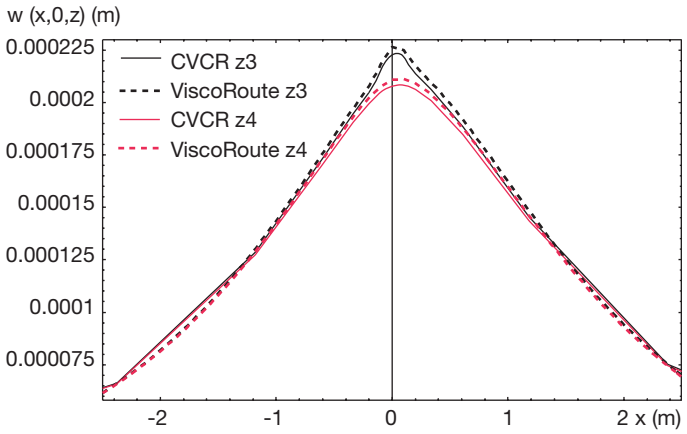

Figure 7

Comparison between CVCR and ViscoRoute at depths z3 = – 0.0165 m and z4 = – 0.37 m

element computation, the target domain is a soil 15 m thick; moreover, 10 m of structure on each side of the load are modeled. Problem symmetry with respect to the xOz plane was employed herein. In order to generate an accurate comparison with the finite elements, a 15-m thick soil layer was introduced into the "ViscoRoute" program, and a solid with a very high Young's modulus value was positioned below this layer to simulate a stiff boundary condition, like for the finite element computation. Results are presented for depths z3 = –0.0165 m and z4 = –0.37 m.

The comparison between results obtained by means of finite element computation and ViscoRoute output is highly satisfactory. If the soil were modeled by a semi-infinite solid, results would be less promising [9], which signifies that the finite element computation contains an extension in Z incapable of fully representing a semi-infinite solid.

Influence of load speed

Given that the model incorporates material viscoelasticity, structural response varies with load speed, as opposed to the purely-elastic case. The computed structure comprises three layers and is identical to the one in the previous section with a semi-infinite solid instead of the 15 m of soil. Figure 8 displays displacements for the case of the three-layer structure with load speeds of 0.1 m/sec, 5 m/sec and 30 m/sec. It may be observed that displacements rise as load speed decreases, due

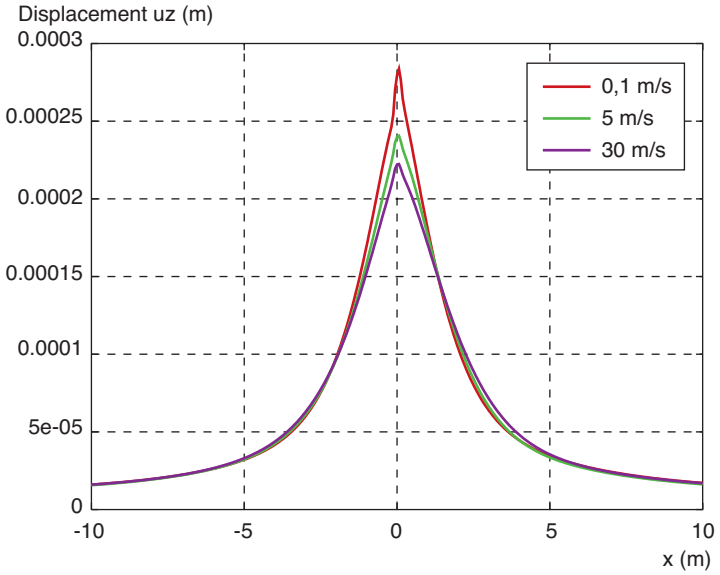

Figure 8
Vertical displacement at depth 0.0165 m for various load speeds

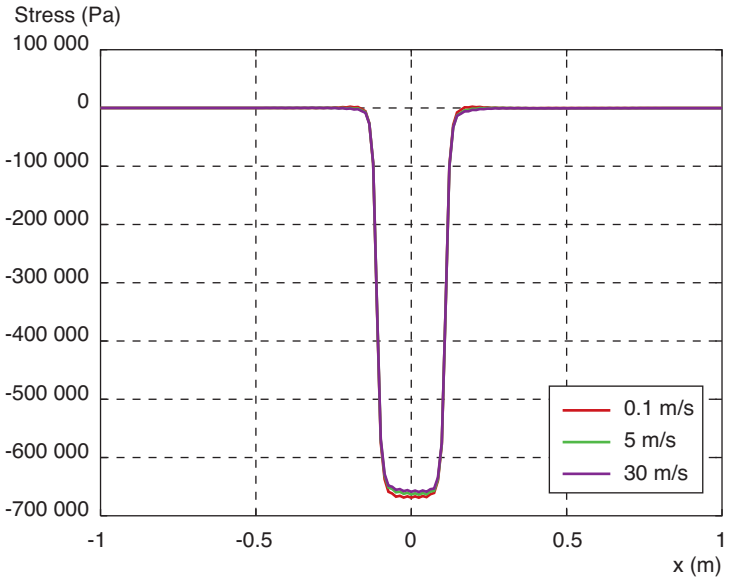

Figure 9
Vertical stress σ_{zz} at depth 0.0165 m for various load speeds

perhaps to the type of dependence inherent in the complex modulus in relation (1), where it is obvious that the modulus becomes higher when speed increases (i.e. by replacing ω with k_1V in the equation). This effect heightens as the load nears. The difference in displacement between the slowest and fastest speeds lies on the order of 30%. Figure 9 shows the influence of speed on vertical stress σ_{zz}; it can be remarked that the variation in stress with speed is small. Stress is primarily concentrated underneath the load.

Influence of temperature

Using the same data as for the previous example, temperature is modified by being ascribed the values 0°C, 15°C and 30°C. Load speed is set at 5 m/sec and the structure is unchanged from the previous section. The corresponding results have been indicated in Figure 10. Viscoelasticity leads to major differences as temperature rises: high temperatures induce large displacements. This effect is

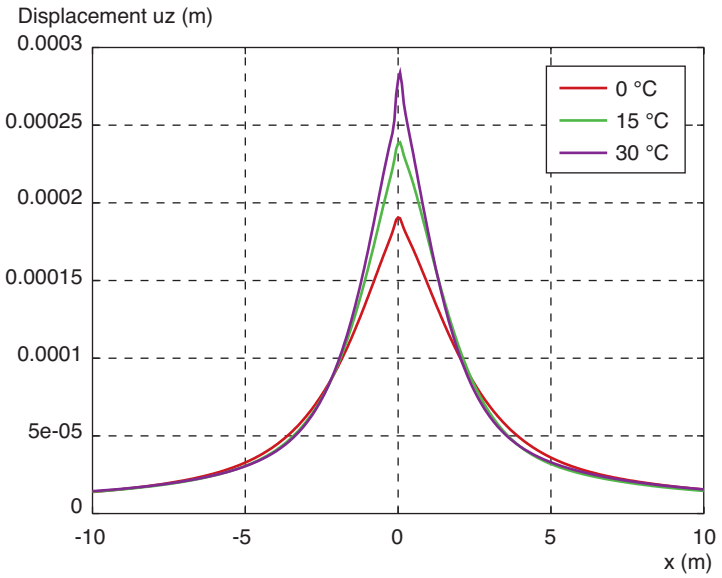

Figure 10
Vertical displacement at depth 0.0165 m vs. temperature

more pronounced than the load speed effect and leads to a 50% increase in displacement for a temperature transition from 0° to 30°C. This finding can be explained by material softening during a temperature rise. As seen with speed, the influence of temperature on stresses remains minimal.

Comparison with measurement readings

The final example focuses on the case of a three-layer structure whose load corresponds to a dual-wheel load distributed over a surface of two rectangles with dimensions: a = 0.15 m and b = 0.09 m (see Fig. 11). Total load equals 65 kN and the speed is 67.8 km/hr. The structure is composed of a semi-coarse asphalt viscoelastic layer 0.085 m thick with the following parameters: $\nu = 0.25$, $E_0 = 70$ MPa, $E\infty = 34{,}000$ MPa, $k = 0.22$, $h = 0.65$, $\delta = 2.8$, $A_0 = 1.94$, $A_1 = -0.373$, $A_2 = 0.00191$, and $\theta = 11.4$°C. This layer lies on top of an unbound granular material layer (0/20 mm) with presumed elastic behavior, a thickness of 0.43 m and parameters $\nu = 0.35$ and E = 130 MPa. Beneath, the solid is presumed to be semi-infinite, corresponding to a type 1 support platform, presumed elastic and with characteristics of E = 40 MPa and $\nu = 0.35$. Results are shown along the *x*-axis positioned halfway between the two loads.

Results are given on Figure 12 for the longitudinal strain ε_{xx} and on Figure 13 for lateral strain ε_{yy}; both these strains are compared with the experimental values obtained from measurements conducted on the LCPC Pavement Fatigue Carrousel (see [14,15]). Curves L11 through L17 on Figure 12 correspond to the longitudinal strain gauges (along *x*) placed at the base of the overlay. The numbers indicate various locations on the fatigue carrousel at the same radius and depth. Similarly,

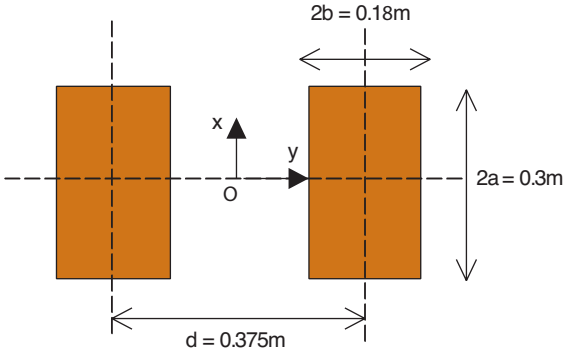

Figure 11
Load characteristics

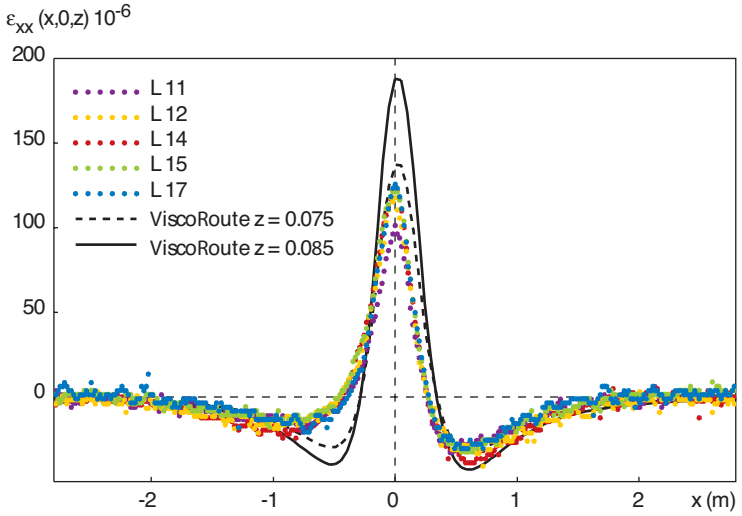

Figure 12
Comparison of longitudinal strain ε_{xx} at depth 0.085 m

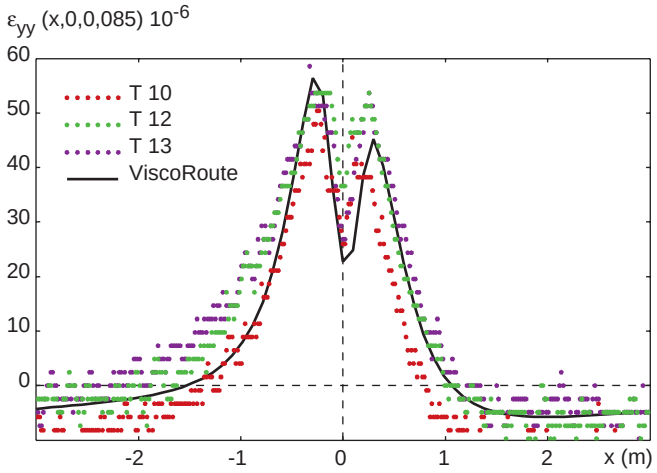

Figure 13
Comparison of transversal strain ε_{yy} at depth 0.085 m

curves T10 to T13 on Figure 13 display the results measured by gauges along the transverse direction (i.e. along *y*). They have also been placed at the overlay base, along the *y*-axis. While a few differences can be detected between model and measurements, the level of agreement is, on the whole, quite satisfactory. These differences can be explained by thickness uncertainties, the various layer moduli, and by soil behavior that might differ from the elastic model used (in particular by its non-linearity).

Conclusion

In conjunction with the problems raised in new pavement design, for which approximating fields by means of computations in linear elasticity proves (in the vast majority of cases) entirely sufficient, a real need for more specialized numerical tools is now felt when it comes to analyzing certain phenomena not incorporated into the set of conventional tools.

In the case of flexible pavements submitted to strong temperature gradients or to the action of slow-speed channeled loads, pavement design fields become asymmetrical and their maximum value may be significantly increased. As such, and this phenomenon does not get highlighted in elastic computations, the strains transverse to the rolling axis may be of greater intensity than the longitudinal strains. This effect has been illustrated effectively in the case of airport runway pavements [3].

A semi-infinite multilayer structure model that incorporates Huet and Sayegh's thermoviscoelastic constitutive law has been developed and programmed in a software application called "ViscoRoute". Computations have been successfully validated thanks to comparison with analytical results for a homogeneous half-space [12], numerical computations obtained from the CESAR-LCPC code's CVCR module, and lastly with experimental results. The chief benefit inherent in ViscoRoute computations is an extremely high-speed execution (typically requiring just a few seconds for a multilayer structure) as opposed to finite element computations.

References

[1] BURMISTER D.M., The theory of stresses and displacements in layered systems and applications of the design of airport runways, *Proceedings of the Highway Research Board*, **23, 1943,** pp. 126-148.

[2] AUTRET P., BAUCHERON de BOISSOUDY A., MARCHAND J.-P., ALIZÉ III Practice, P*roc. 5th int. Conf. Structural Design of Asphalt Pavements*, Delft, **1982,** pp. 174-191.

[3] VILA B., *Modélisation numérique des structures de chaussées souples en viscoélasticité et première modélisation des chaussées rigides – Pavement experimental program Airbus à Toulouse-Blagnac*, Rapport de stage de fin de 2e année d'ingénieur à l'INSA de Toulouse, **2001.**

[4] TAMAGNY Ph., WENDLING L., PIAU J.-M., A new explanation of pavement cracking from top to bottom : the visco-elasticity of asphalt materials, *Proceedings of the Fifth International RILEM Conference Cracking in Pavements,* Limoges, France, May 5-8, **2004,** pp. 425-432.

[5] HUET C., *Étude par une méthode d'impédance du comportement viscoélastique des matériaux hydrocarbonés*, Thèse de doctorat ès sciences, Faculté des sciences de Paris, **1963.**

[6] SAYEGH G., Variation des modules de quelques bitumes purs et bétons bitumineux, *Conférence au Groupe français de Rhéologie*, **1963,** pp. 51-74.

[7] NGUYEN V.H., *Comportement dynamique de structures non linéaires soumises à des charges mobiles*, Thèse de doctorat ès sciences, ENPC, Champs-sur-Marne, **2002.**

[8] DUHAMEL D., NGUYEN V.H., CHABOT A., TAMAGNY Ph., Modelling of multilayer viscoelastic road structures under moving loads, paper 79, *Ninth international conference on civil & structural engineering computing*, Egmond aan Zee, The Netherlands, 2-4 September **2003.**

[9] DUHAMEL D., NGUYEN V.H., CHABOT A., TAMAGNY Ph., Modélisation de chaussées viscoélastiques, *16e Congrès français de Mécanique, CFM*, Nice, 1-5 septembre **2003**.

[10] CHAILLEUX E., *ViscoAnalyse : un logiciel de traitement des données viscoélastiques des matériaux bitumineux et de calibrage du modèle de Huet-Sayegh*, logiciel en cours de validation - emmanuel.chailleux@lcpc.fr, **2005.**

[11] JOHNSON K.L., *Contact mechanics*, Cambridge University Press, **1992.**

[12] CHABOT A., PIAU J.-M., Calcul semi-analytique d'un massif viscoélastique soumis à une charge roulante rectangulaire, *1re Conférence internationale Albert Caquot*, Paris, octobre **2001.**

[13] HECK J.V., PIAU J.-M., GRAMSAMMER J.-C., KERZREHO J.-P., ODÉON H., Thermoviscoelastic modelling of pavement behaviour and comparison with experimental data from LCPC test track, *5th Conference on Bearing Capacity of Roads and Airfields*, Trondheim, Norway, **1998.**

[14] HORNYCH P., KERZREHO J.-P., SALASCA S., Prediction of the behaviour of a flexible pavement using finite element analysis with non-linear elastic and viscoelastic models, *ISAP*, Copenhaguen, August **2002.**

[15] DE LA ROCHE C., CORTÉ J.-F., GRAMSAMMER J.-C., ODÉON H., TIRET L., CAROFF G., Étude de la fatigue des enrobés bitumineux à l'aide du manège de fatigue du LCPC, *Revue Générale des Routes et Aérodromes*, **716,** mars **1994,** pp. 62-74.